Nonlinear Wave Growth of Whistler-mode Hiss Emissions in a Uniform Magnetic Field

Yin Liu[1], **Yoshiharu Omura**[1]

[1] Research Institute for Sustainable Humanosphere, Kyoto University, Kyoto, Japan.

Key Points:

- Coherent whistler-mode hiss wave packets can grow from thermal fluctuations in the equatorial plasmasphere.
- Nonlinear wave growth processes due to frequency variation take place with the coherent hiss wave packets.
- The nonlinear growth rates of hiss with rising and falling tones are much greater than the linear growth rates.

Corresponding author: Y. Omura, omura@rish.kyoto-u.ac.jp

Abstract

We conduct electromagnetic particle simulations in a uniform magnetic environment to verify the nonlinear wave growth process of plasmaspheric hiss in the equatorial plasmasphere. The satisfaction of the separability criterion for coexisting multiple frequency waves in the initial stage of wavenumber-time evolution declares that wave packets are coherent and capable of growing nonlinearly. Spatial and temporal evolutions of two typical modes located in wavenumber-time evolution demonstrate the consistency among wave growths, frequency variations, and inhomogeneity factor S in coherent wave packets, showing that rising and falling tones occur at negative and positive S values, respectively, and an obvious wave growth happens in a reasonable range of S satisfying the second-order resonance condition. Wave packets extracted from wave fields in space and time by band-pass filter confirm good agreement between nonlinear theory and simulation results. The nonlinear growth rates of the extracted wave packets posses similar magnitudes to the growth rates of wave packets in the simulation, and they are much greater than the theoretical linear growth rate, indicating that the nonlinear process is essential in the generation of plasmaspheric hiss.

1 Introduction

Plasmaspheric hiss emissions, as a type of whistler-mode wave, possess a typical frequency range from ~ 100Hz to several kHz and an amplitude range from a few pT to hundreds of pT. They widely occur in the Earth's inner magnetosphere and play a key role in controlling the balance of high-energy particles injected and lost from in the near-Earth environment (e.g. *Breneman et al.* [2015]; *Li et al.* [2014]; *Meredith et al.* [2006]; *Summers et al.* [2007a,b]). Since the energetic electrons may cause damage to spacecrafts and satellites, it is important to understand the generation process of hiss emissions. In the past few decades, several generation mechanisms of hiss based on the linear growth theory (*Kennel and Petschek* [1966]) are proposed, among which the main difference lies on whether seeds of the instability derive inside or outside of the plasmaphere. For instance, *Draganov et al.* [1992] proposed that lighting strikes inside atmosphere may cause the generation of whistler-mode hiss; *Bortnik et al.* [2008] suggested that chorus waves that have leaked inside the plasmasphere can evolve into hiss emissions; *Chen et al.* [2014] suggested that the ULF plasmapheric hiss may grow from the internal thermal fluctuations.

Summers et al. [2014] first identified and examined the embedded fine structures of plasmaspheric hiss based on the high-resolution data from the Van Allen Probes EMFISIS

(Electric and Magnetic Field Instrument Suite and Integrated Science) instrument, showing that hiss emissions considered as structureless and incoherent for a long time actually possess short rising and falling tone structures similar to the sub-packets of chorus. Inspired by this, *Omura et al.* [2015] proposed the nonlinear wave growth theory of coherent hiss emissions, claiming that the generation of plasmaspheric hiss shares the similar mechanism that was originally used in explaining the generation of whistler-mode chorus. *Nakamura et al.* [2016] further found good agreements between observed frequency sweep rates for rising tone elements and the nonlinear theory while applying the theory to hiss emissions. *Hikishima et al.* [2020] succeeded in reproducing hiss emissions in electromagnetic particle simulations that follow the nonlinear wave growth theory. *Liu et al.* [2021] varied key parameters in both simulations and theory, verified the applicability of the nonlinear theory on the generation of plasmaspheric hiss. They have clarified the effect of the gradient of the magnetic field on the nonlinear wave growth process. However, it was not clear if the inhomogeneous magnetic field is essentail for generation of plasmaspheric hiss.

To further examine the details of the nonlinear wave growth process of hiss, we assume a uniform background magnetic field in the simulation, and analyze the consistency between the theory and simulation results. We describe our simulation model in section 2. We present our analysis on the simulation results in section 3. We give summary and discussion in section 4.

2 Simulation Model

The code of the self-consistent electromagnetic particle simulations employed in this study originates from KEMPO (Kyoto university ElectroMagnetic Particle cOde) deployed by *Matsumoto and Omura* [1985] and *Hikishima et al.* [2009]. Specifically, we implemented a one-dimensional model with 32768 grids for the entire system, an open boundary condition and a damping region at each side to handle the outgoing waves. With reference to *Umeda et al.* [2001], the range of one damping region is set to 6.25% system length. We initialize two species of cold and hot electrons in the system. For cold electrons, we let them obey a Maxwellian distribution with small thermal velocities. For hot electrons, we assume a subtracted Maxwellian momentum distribution function with parallel and perpendicular momenta $U_{th\parallel} = 0.26c$ and $U_{th\perp} = 0.3c$, respectively, yielding an initial temperature anisotropy around 0.72, as shown in Figure 1a. Here, c represents speed of light. Figure 1b illustrates the variation of velocity distribution of hot electrons at $t = 20480\Omega_{e0}^{-1}$. In the simulations,

particles lost into loss cone are counted as missing, corresponding to the depletion at low pitch angle area in Figure 1b. The obvious depletion at high pitch angle part in the figure represents that hot electrons transfer energy to waves through wave-particle interactions. Both cold and hot electrons are allocated uniformly in the entire system region. The plasma frequencies of hot and cold electrons are set to $\omega_{ph} = 0.3\Omega_{e0}$ and $\omega_{pe} = 15\Omega_{e0}$, respectively, where Ω_{e0} is the gyrofrequency of an electron at the equator. In the simulations, the charge of an electron is given by

$$q = \frac{\epsilon_0 \omega_p^2}{(q/m)n}, \tag{1}$$

where ϵ_0 is the permittivity of free space; ω_p, n, and m represent plasma frequency, number density, and mass of a hot or cold electron, respectively. Since the charge-to-mass ratio q/m is constant in electromagnetic particle simulations, to ensure that the electromagnetic thermal fluctuation (i.e., $0.5mv_{th\perp}^2$) is determined by the hot electrons rather than the cold electrons, a very small thermal velocity and a large number of super-particles are set for cold electrons. The key parameters are listed in Table 1. Under the simulation settings, dynamic spectra of overall and separated waves propagating forward and backward at different locations are shown in Figure 2, in which the amplitude and frequency ranges of the waves are close to the observed hiss emissions in plasmasphere, and clear falling and rising tones can be found.

3 Results

3.1 Wave packet coherency

The nonlinear wave growth theory only suits for coherent wave packets. *Omura et al.* [2015] provided a criterion of separability of each coherent wave packet from coexisting wave pakcets to examine wave packet coherency, i.e.,

$$|\omega_{j+1} - \omega_j| \gg \Delta\omega, \tag{2}$$

where ω_{j+1} and ω_j represent frequencies of two frequency-adjacent waves at the same space and time, $\Delta\omega$ is the frequency bandwidth corresponding to the size of the trapping potential in velocity phase space and expressed as Equation (110) in *Omura* [2021]. In the model of the uniform background magnetic field and plasma density, to see whether (2) is satisfied in the simulations, we can check the correlation between wavenumber k and wavenumber bandwidth Δk shown below in the initial stage, avoiding the difficulty in examining $\Delta\omega$ directly,

$$|k_{j+1} - k_j| \gg \Delta k, \tag{3}$$

where we use the vroup velocity V_g of the whistler-mode waves to convert $\Delta\omega$ to Δk by $\Delta k = \Delta\omega/V_g$.

Figure 3 gives the wavenumber-time evolution of amplitudes B_w and Δk for forward-propagating waves within $t = 0 \sim 5000\Omega_{e0}^{-1}$ and $k = 3.03 \sim 3.76c^{-1}\Omega_{e0}$ in two panels, respectively. In Figure 3a, three typical modes are found and labeled, the corresponding wavenumber values are $k_1 = 3.0488c^{-1}\Omega_{e0}$, $k_2 = 3.2214c^{-1}\Omega_{e0}$, and $k_3 = 3.3557c^{-1}\Omega_{e0}$, respectively. To check the relation (3), proper values of $\Delta k_j, j = 1, 2$ need to be chose on the first two labeled modes in Figure 3b.

Since wave packets are generated from thermal noises due to frequency variation according to the nonlinear wave growth theory, we try to find moments where frequency variations first take place in the selected modes as their generation time, and choose the corresponding Δk there. In wavenumber-time evolution, a wavenumber shift is related to frequency variation. In Figure 4, we find an obvious right shift of wavenumber from the left adjacent mode to the first selected mode at around $t = 750\Omega_{e0}^{-1}$, as indicated by the black arrow in Figure 4a. Similarly, a left shift from the second selected mode to its left adjacent mode is found at $t = 1250\Omega_{e0}^{-1}$ in Figure 4b, as indicated by the red arrow. Referring to Equation (87) in *Omura* [2021] together with the approximate amplitude and wavenumber information, we obtain a quarter of the nonlinear trapping time for the first two selected modes around $830\Omega_{e0}^{-1}$ and $494\Omega_{e0}^{-1}$, respectively. The values are close to the time duration of the wavenumber shifts in Figure 4, indicating trapping potentials are formed and nonlinear wave growth process takes place within the time range. Therefore, $750\Omega_{e0}^{-1}$ and $1250\Omega_{e0}^{-1}$ can be considered as the approximate generation time of the first and second selected modes in Figure 3. The corresponding Δk values at their generation time in Figure 3b are $\Delta k_1 = 0.0314c^{-1}\Omega_{e0}$ and $\Delta k_2 = 0.0504c^{-1}\Omega_{e0}$, respectively. Since $k_2 - k_1 = 0.1726 \gg \Delta k_1$ and $k_3 - k_2 = 0.1343 \gg \Delta k_2$, the separability criterion (3) is satisfied, and the coherency of wave packets in hiss simulations is thus verified.

Note that the analysis in k-space does not contain the space information of wave packets, while the coherency discussed in the nonlinear theory should concentrate on a fixed space. Therefore, the separability that Δk represents may slightly differ from that represented by $\Delta\omega$ due to the transform from space-time to wavenumber-time evolution.

3.2 Wavenumber-time evolution

In a uniform background magnetic environment, the inhomogeneity factor S is simplified to

$$S = -\frac{1}{s_0 \omega \Omega_w} s_1 \frac{\partial \omega}{\partial t}, \tag{4}$$

where Ω_w is wave amplitude given by qB_w/m, $\partial\omega/\partial t$ represents wave frequency variation, and parameters s_0 and s_1 are expressed as Equations (38) and (39) in *Omura* [2021], respectively. Therefore, the nonlinear process is determined by the frequency variation in a uniform magnetic environment.

The frequency variation relates to the wavenumber shift in wavenumber-time evolution of wave amplitudes. In Figure 5, we locate two typical modes assumed as M_1 and M_2 in wavenumber-time evolution of amplitudes for forward-propagating waves, respectively, as indicated by the two pink rectangles. Specifically, M_1 possesses a time range of $1044.97 \sim 1387.60\Omega_{e0}^{-1}$ and a wavenumber range of $2.95 \sim 3.01 c^{-1}\Omega_{e0}$. The left-shift trend of the wavenumber declares that wave packets in M_1 tend to be falling-tone. For M_2, it has a time range of $1314.37 \sim 1513.14\Omega_{e0}^{-1}$ and wavenumber range of $3.20 \sim 3.27 c^{-1}\Omega_{e0}$. Since wavenumber in M_2 shifts to right, the corresponding wave packets are more likely rising-tone.

Figure 6 gives the corresponding space-time evolution of amplitudes, frequencies, S values, and J_B/B_w in M_1, where a band-pass filter corresponds to the wavenumber range of M_1 is applied. Here, J_B represents the component of resonant current parallel to the magnetic field of wave and affects the wave frequency variation in a nonlinear wave growth process through the relation

$$\delta\omega = -\frac{\mu_0 V_g}{2} \frac{J_B}{B_w}, \tag{5}$$

where μ_0 is the permeability of free space. In Figure 6a, two obvious wave packets are found in M_1, and the right packet is dominant due to its large amplitudes. In each panel, the approximate end of the right packet is indicated by the dashed line. In Figure 6b, the frequency at the end area of the right packet decreases, thus a falling tone is formed there, determining the left shift of wavenumber in M_1. According to (4) and (5), as the wave frequency decreases, i.e., $\partial\omega/\partial t < 0$, both values of S and J_B/B_w should be positive. In Figures 6c and 6d, we do find the same results near the end area of the right packet, showing a good agreement between the theory and simulations.

It is also noted that an obvious fluctuation of S values from positive to negative occurs after the wave packet on the right, as shown in Figure 6c. This indicates that new wave-particle interaction occurs, leading to the formation of new resonant currents. The newly formed resonant currents may suddenly vary the symbol of old J_B, thus the symbol of frequency variation $\delta\omega$ suddenly changes according to (5), causing the sudden change of S values through the relation (4).

Figure 7 gives the dynamic spectra at $h = 125c\Omega_{e0}^{-1}$ for forward-propagating waves and packets in M_1, respectively. In Figure 7b, an obvious falling-tone structure is identified, which agrees with the preceding discussions.

Similarly, based on the information of M_2, the space-time evolution is obtained, as shown in Figure 8. The right wave packet is dominant in the two packets found in Figure 8a, it also determines the right shift of wavenumber in M_2 because the frequency at its end area increases obviously in Figure 8b. The values of S and J_B/B_w at the end of the right packet in Figures 8c and 8d are positive accordingly. In Figure 9, we locate the rising-tone structure corresponding to M_2 in the dynamic spectrum at $h = 75c\Omega_{e0}^{-1}$.

It is worth noting that a gap exists between the two wave packets in Figure 8a, where obvious fluctuations of S values happen several times in Figure 8c, meaning that new wave-particle actions take place there. However, no wave packets are generated in the area. This is reasonable because the quantities of S are too large there, while optimum wave growth should happen at around $|S| = 0.4$. Another explanation relates to the sign of J_E representing the component of the resonant current parallel to the electric field of the wave. From the contribution of J_E to the wave evolution, i.e.,

$$\frac{\partial B_w}{\partial t} + V_g \frac{\partial B_w}{\partial h} = -\frac{\mu_0 V_g}{2} J_E, \tag{6}$$

where $\partial B_w/\partial t$ and $\partial B_w/\partial h$ represent the wave growth along time and space, respectively, wave growth only occurs when J_E is negative. Therefore, although wave-particle interactions exist between the two packets in Figure 8a, most values of J_E there are positive, as illustrated in Figure 10. Waves are being damped, whereas electrons are accelerated in this area.

3.3 Space-time evolution

While multiple wave packets are generated at different frequencies at the same time and position, we have extracted a single wave packet in the space-time evolution by the fol-

lowing method. Figure 11 illustrates the space-time evolution of amplitudes for waves propagating forwardly along a uniform background magnetic field after applying a band-pass filter of $0.04 \sim 0.06\Omega_{e0}$. In the figure, a typical wave packet is extracted by locating its center (indicated by the white dotted line) together with a spatial width of the packet on each side (indicated by the red lines).

Using the extracted wave packet, we obtain amplitudes, frequencies, frequency variations, S values, nonlinear growth rates, and growth rates in the simulation as shown in Figure 12, where vertical and horizontal axes represent the temporal width and spatial information of the extracted packet, and values in the brackets represent the time information of the packet center, i.e., the white dotted line in Figure 11. In Figure 12a, based on a vertical analysis (i.e., along time at a fixed position), the parts close to the end of the wave packet (i.e., the upper parts with $\Delta T > 0$) undergoes an obvious growth at around $h = 0c\Omega_{e0}^{-1}$, and the growth quickly spreads to the front parts of the packet (i.e., the lower parts with $\Delta T < 0$) as it propagates. At around $h = 100c\Omega_{e0}^{-1}$, the whole packet has relatively large amplitudes. According to (6), a rapid wave growth in space and time relates to a large magnitude of $-J_E$, further representing that a reasonable value of S ($|S| < 1$) occurs in the area from the relation in Figure 3 of *Omura* [2021]. In Figure 12d, we do find the parts close to the area where the quick growth of the wave amplitudes occurs possess more reasonable S values, indicating that it is $-J_E$ contributing to the wave growth, and the nonlinear process happens there. In Figures 12b and 12c, when the wave packet is at upstream, i.e., $h < 100c\Omega_{e0}^{-1}$, from a vertical view, the frequency at a fixed position tends to decrease at its front part and increase at its end part. However, as it propagates to the downstream, i.e., $h > 100c\Omega_{e0}^{-1}$, the frequency increases first and then decreases at a fixed position. Since the direction of frequency variation is determined by the symbol of J_B according to (5), the results imply that J_B changes from positive to negative at upstream, while negative to positive at downstream. The trend is well illustrated in Figure 12d because S value follows the same symbol as J_B. The nonlinear growth rates in Figure 12e are based on Equation (92) in *Omura* [2021], while the growth rates in the simulation in Figure 12f are computed from two adjacent wave amplitudes B_{w1} and B_{w2} inside one wave packet, i.e.,

$$\Gamma_C = \ln\left(\frac{B_{w2}}{B_{w1}}\right)\frac{V_g}{\Delta h}, \tag{7}$$

where Δh represents the spatial distance between two amplitudes. In addition, the theoretical linear growth rate indicated by the red arrows is calculated by the KUPDAP (Kyoto University Plasma Dispersion Analysis Package) developed by *Sugiyama et al.* [2015]. The result

implies that linear growth rate is much smaller than the nonlinear growth rates in the area where wave amplitudes grow rapidly in Figure 12a, and the nonlinear growth rates possess a similar form to the growth rates in the simulation, indicating that the nonlinear wave growth process is dominant in the wave growth.

Although the extraction of wave packets in space-time evolution verifies the nonlinear process, the method has difficulty in choosing a proper frequency range for the band-pass filter to maintain the coherency of wave packets. Since the range of $0.04 \sim 0.06\Omega_{e0}$ applied in Figure 12 is relatively large, several wave packets with different frequencies actually exist in the extracted packet. Therefore, frequency variations and sudden changes of S values happen inside the extracted wave packet in Figures 12b, 12c, and 12d. The magnitude of S values also tend to be large due to large frequency variations.

4 Summary and Discussion

We have conducted an electromagnetic particle simulation in a uniform background magnetic environment to examine the nonlinear wave growth process in the generation of plasmaspheric hiss. Our findings are summarized below,

1. The coherency of wave packets generated in the hiss simulations is satisfied by checking the separability criterion in the initial stage of wavenumber-time evolution;
2. The nonlinear wave growth process is verified by checking consistency among wave growths, frequency variations, and S values in the coherent wave packets located in wavenumber-time evolution;
3. The theoretical nonlinear growth rates possess similar magnitudes to the growth rates of the extracted wave packet in the simulation, and they are much greater than the linear growth rate, indicating that nonlinear wave growth process due to frequency variations is essential in the generation of plasmaspheric hiss.

The analysis on the extracted wave packet reveals the complexity of choosing the proper range of a band-pass filter because plasmaspheric hiss tends to be short in space and time. In addition, the existence of merging and splitting processes makes it even harder to maintain the coherency of wave packets while applying the band-pass filter. For example, Figure 13 illustrates a part of the dynamic spectrum for forward-propagating waves within $10159 \sim 15123\Omega_{e0}^{-1}$ at $h = 100c\Omega_{e0}^{-1}$. There exist clear frequency splitting and merging as indicated by

the white arrows. Specifically, the splitting of one wave packet indicates that probably both electron hole and hill are formed in one wave-particle interaction process, while the merging of two wave packets may be related to the effect of coalescence of two nonlinear wave potentials in the velocity phase space as we observed in the nonlinear evolution of electron beam instabilities (*Omura et al.* [1996]). In any case, the coherency of wave packets is challenged, because a stable single wave potential is not guaranteed in the splitting and merging processes.

Another complementary discussion is on the probability of generating a rising or a falling tone. At $h = 100c\Omega_{e0}^{-1}$, we have a rough statistics of 47 rising tones and 39 falling tones after applying a band-pass filter of $0.04 \sim 0.06\Omega_{e0}$, indicating that they have similar chances to take place. Moreover, the occurrence of a rising or falling tone tends to be random in time. This can be preliminarily explained by the fact that a positive or negative J_B is determined by the value of ζ when an wave potential is formed, while ζ representing an angle between the magnetic component of the wave field and the perpendicular velocity of a resonant electron is not predictable before they encounter.

As future studies, a theoretical model suitable for falling-tone hiss is necessary for describing a complete nonlinear wave growth process in a parabolic magnetic field, and the precipitation or nonlinear scattering of energetic elections by coherent plasmaspheric hiss is also an interesting research topic.

Data Availability Statement

The simulation data files and a sample program to read the data files are open to the public at the web (https://zenodo.org/record/6277653). The simulation data used in this paper are obtained from KEMPO1 code (https://space.rish.kyoto-u.ac.jp/software/).

Acknowledgments

The computer simulation in the present study was performed on the KDK computer system at Research Institute for Sustainable Humanosphere, Kyoto University. This work was supported by JSPS KAKENHI Grant Number JP17H06140.

References

Bortnik, J., R. M. Thorne, and N. P. Meredith (2008), The unexpected origin of plasmaspheric hiss from discrete chorus emissions, *Nature*, *452*(7183), 62–66.

Breneman, A., A. Halford, R. Millan, M. McCarthy, J. Fennell, J. Sample, L. Woodger, G. Hospodarsky, J. Wygant, C. Cattell, et al. (2015), Global-scale coherence modulation of radiation-belt electron loss from plasmaspheric hiss, *Nature*, *523*(7559), 193–195.

Chen, L., R. M. Thorne, J. Bortnik, W. Li, R. B. Horne, G. Reeves, C. Kletzing, W. Kurth, G. Hospodarsky, H. E. Spence, et al. (2014), Generation of unusually low frequency plasmaspheric hiss, *Geophysical Research Letters*, *41*(16), 5702–5709.

Draganov, A., U. Inan, V. Sonwalkar, and T. Bell (1992), Magnetospherically reflected whistlers as a source of plasmaspheric hiss, *Geophysical research letters*, *19*(3), 233–236.

Hikishima, M., S. Yagitani, Y. Omura, and I. Nagano (2009), Full particle simulation of whistler-mode rising chorus emissions in the magnetosphere, *Journal of Geophysical Research: Space Physics*, *114*(A1).

Hikishima, M., Y. Omura, and D. Summers (2020), Particle simulation of the generation of plasmaspheric hiss, *Journal of Geophysical Research: Space Physics*, *125*(8), e2020JA027,973.

Kennel, C. F., and H. Petschek (1966), Limit on stably trapped particle fluxes, *Journal of Geophysical Research*, *71*(1), 1–28.

Li, W., B. Ni, R. Thorne, J. Bortnik, Y. Nishimura, J. Green, C. Kletzing, W. Kurth, G. Hospodarsky, H. E. Spence, et al. (2014), Quantifying hiss-driven energetic electron precipitation: A detailed conjunction event analysis, *Geophysical Research Letters*, *41*(4), 1085–1092.

Liu, Y., Y. Omura, and M. Hikishima (2021), Simulation study on parametric dependence of whistler-mode hiss generation in the plasmasphere, *Earth, Planets and Space*, *73*(1), 1–17.

Matsumoto, H., and Y. Omura (1985), Particle simulation of electromagnetic waves and its application to space plasmas, *Computer Simulation of Space Plasmas*, *43*, 43–102.

Meredith, N. P., R. B. Horne, S. A. Glauert, R. M. Thorne, D. Summers, J. M. Albert, and R. R. Anderson (2006), Energetic outer zone electron loss timescales during low geomagnetic activity, *Journal of Geophysical Research: Space Physics*, *111*(A5).

Nakamura, S., Y. Omura, D. Summers, and C. A. Kletzing (2016), Observational evidence of the nonlinear wave growth theory of plasmaspheric hiss, *Geophysical Research Letters*,

43(19), 10–040.

Omura, Y. (2021), Nonlinear wave growth theory of whistler-mode chorus and hiss emissions in the magnetosphere, *Earth, Planets and Space*, *73*(1), 1–28.

Omura, Y., H. Matsumoto, T. Miyake, and H. Kojima (1996), Electron beam instabilities as generation mechanism of electrostatic solitary waves in the magnetotail, *Journal of Geophysical Research: Space Physics*, *101*(A2), 2685–2697.

Omura, Y., S. Nakamura, C. A. Kletzing, D. Summers, and M. Hikishima (2015), Nonlinear wave growth theory of coherent hiss emissions in the plasmasphere, *Journal of Geophysical Research: Space Physics*, *120*(9), 7642–7657.

Sugiyama, H., S. Singh, Y. Omura, M. Shoji, D. Nunn, and D. Summers (2015), Electromagnetic ion cyclotron waves in the earth's magnetosphere with a kappa-maxwellian particle distribution, *Journal of Geophysical Research: Space Physics*, *120*(10), 8426–8439.

Summers, D., B. Ni, and N. P. Meredith (2007a), Timescales for radiation belt electron acceleration and loss due to resonant wave-particle interactions: 2. evaluation for vlf chorus, elf hiss, and electromagnetic ion cyclotron waves, *Journal of Geophysical Research: Space Physics*, *112*(A4).

Summers, D., B. Ni, and N. P. Meredith (2007b), Timescales for radiation belt electron acceleration and loss due to resonant wave-particle interactions: 2. evaluation for vlf chorus, elf hiss, and electromagnetic ion cyclotron waves, *Journal of Geophysical Research: Space Physics*, *112*(A4).

Summers, D., Y. Omura, S. Nakamura, and C. A. Kletzing (2014), Fine structure of plasmaspheric hiss, *Journal of Geophysical Research: Space Physics*, *119*(11), 9134–9149.

Umeda, T., Y. Omura, and H. Matsumoto (2001), An improved masking method for absorbing boundaries in electromagnetic particle simulations, *Computer Physics Communications*, *137*(2), 286–299.

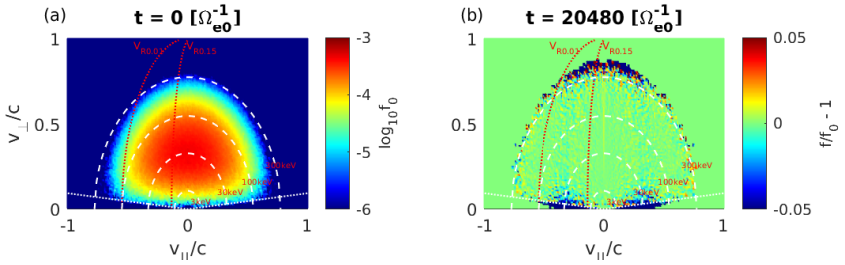

Figure 1. (a) Initial velocity distribution of hot electrons within the entire system region, (b) variation of the velocity distribution at $t = 20480[\Omega_{e0}^{-1}]$. The two red dotted curves represent resonance velocities at wave frequency $\omega = 0.05$ and $0.15\Omega_{e0}$, respectively. The white dashed curves indicate different kinetic energy levels. The white dotted lines denote the range of loss cone.

Table 1. Key simulation parameters

Parameter	Value
Time step: Δt	$0.004\Omega_{e0}^{-1}$
Grid spacing: Δh	$0.01c\Omega_{e0}^{-1}$
System length: h_s	$327.68c\Omega_{e0}^{-1}$
Plasma frequency of cold electrons: ω_{pe}	$15\Omega_{e0}$
Plasma frequency of hot electrons: ω_{ph}	$0.3\Omega_{e0}$
Number of super-particles for cold electrons: $N_{p_{cold}}$	33554432
Number of super-particles for hot electrons: $N_{p_{hot}}$	67108864
Thermal momenta of hot electrons at the equator: $U_{th\parallel}, U_{th\perp}$	$0.28c, 0.30c$

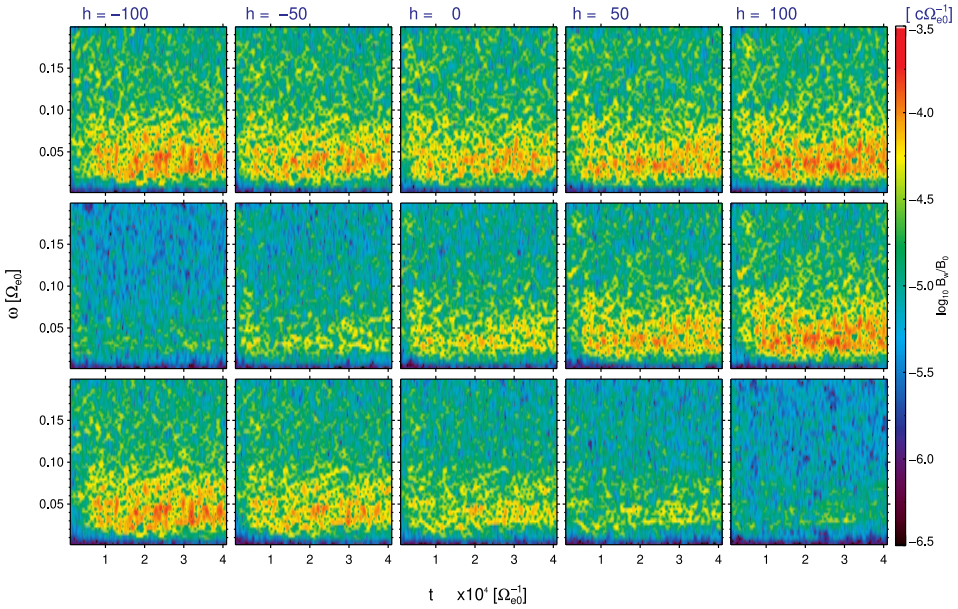

Figure 2. Dynamic spectra for overall waves (top row), forward-propagating waves (middle row), and backward-propagating waves (bottom row) under a uniform background magnetic environment at $h = -100, -50, 0, 50, 100c\Omega_{e0}^{-1}$ within $t = 0 \sim 40960\Omega_{e0}^{-1}$ and $\omega = 0 \sim 0.2\Omega_{e0}$, respectively. $h = 0c\Omega_{e0}^{-1}$ represents the center of the simulation region.

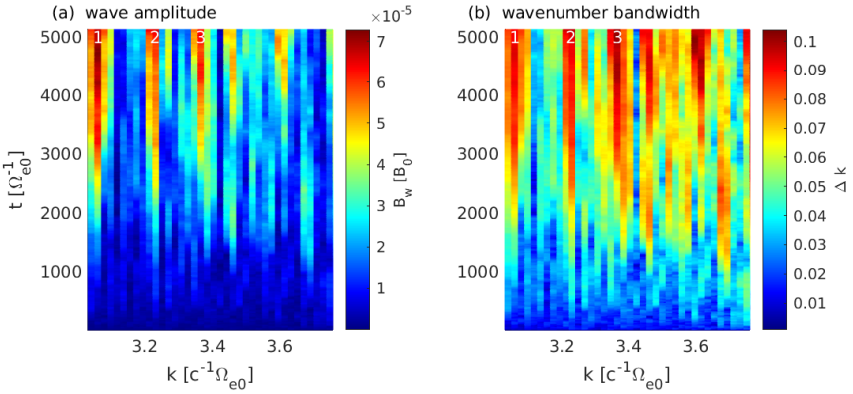

Figure 3. (a) Wavenumber-time evolution of amplitudes for forward-propagating waves ($t = 0 \sim 5000\Omega_{e0}^{-1}$), (b) Δk values corresponding to panel (a). Three typical modes are labeled in both panels for the further analysis.

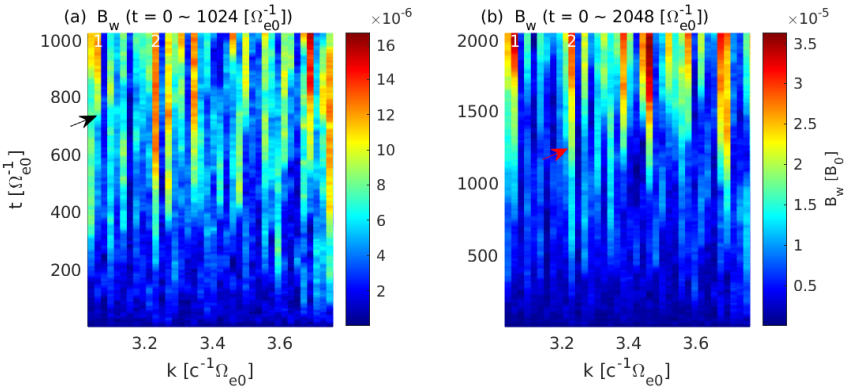

149 **Figure 4.** Wavenumber-time evolution of amplitudes for forward-propagating waves within different time
150 range to find the generation time of the first two modes labeled in Figure 3. The time position indicated by
151 the black arrow in panel (a) (around $750\Omega_{e0}^{-1}$) is considered as the generation time of the first mode; the time
152 indicated by the red arrow in panel (b) (around $1250\Omega_{e0}^{-1}$) is considered as the generation time of the second
153 mode.

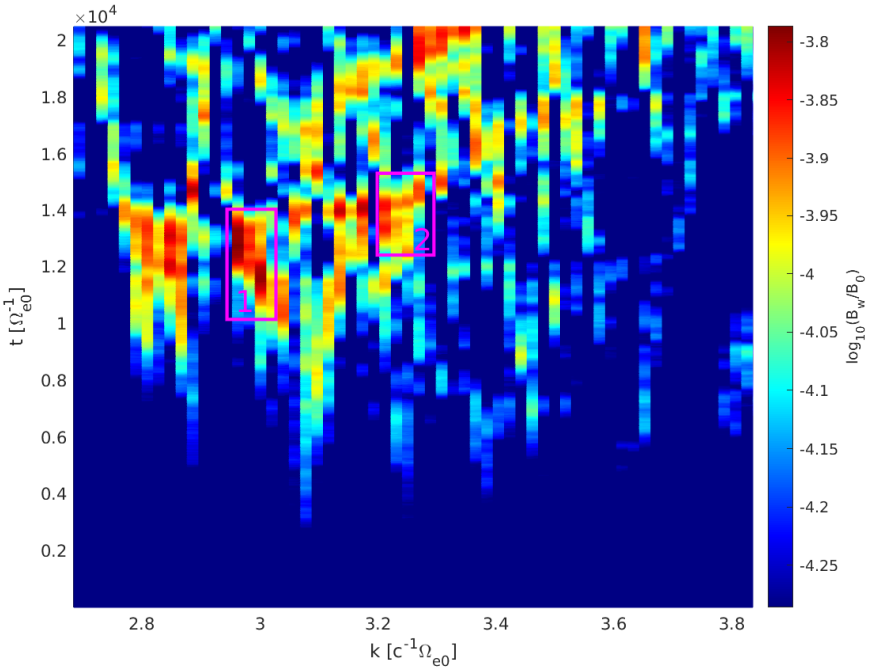

171 **Figure 5.** Wavenumber-time evolution of amplitudes for forward-propagating waves ($t = 0 \sim 20000\Omega_{e0}^{-1}$).
172 Two typical modes are selected for further analyses, as indicated by the pink rectangles. Particularly, the first
173 mode corresponds to a falling-tone property, while the second mode corresponds to a rising-tone property.

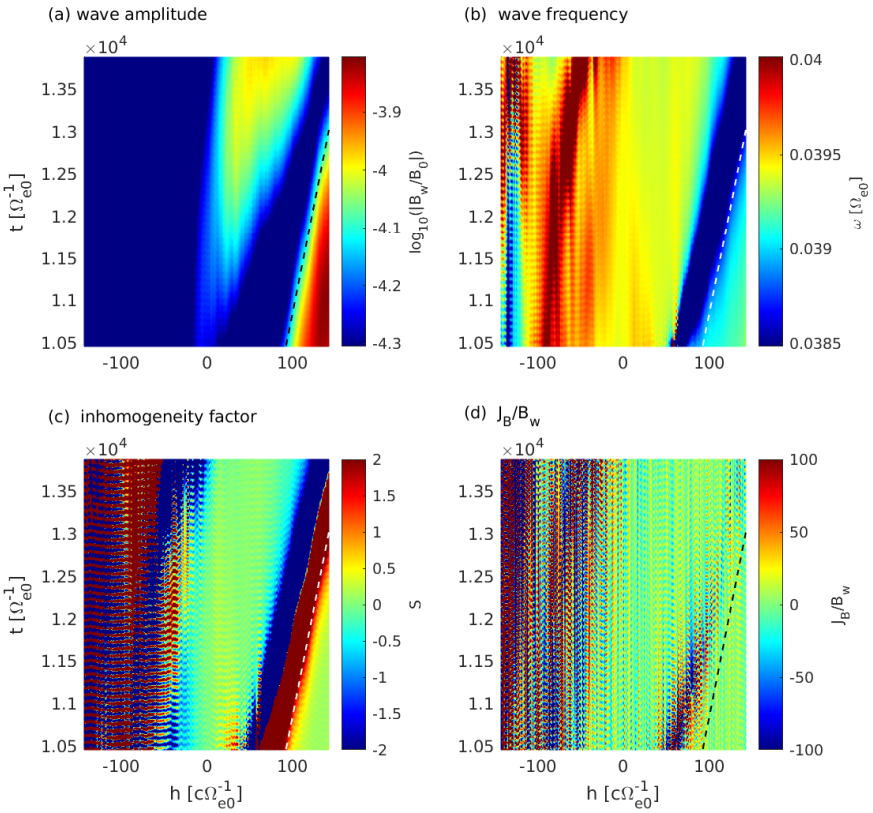

194 **Figure 6.** Spatial and temporal evolution of amplitudes, frequencies, S values, and J_B/B_w for the first
195 selected mode in Figure 5, in which a band-pass filter of $0.038 \sim 0.040\Omega_{e0}$ corresponding to the wavenumber
196 range of the mode is applied. The approximate end of the wave packet on the right is indicated by dashed line
197 in each panel.

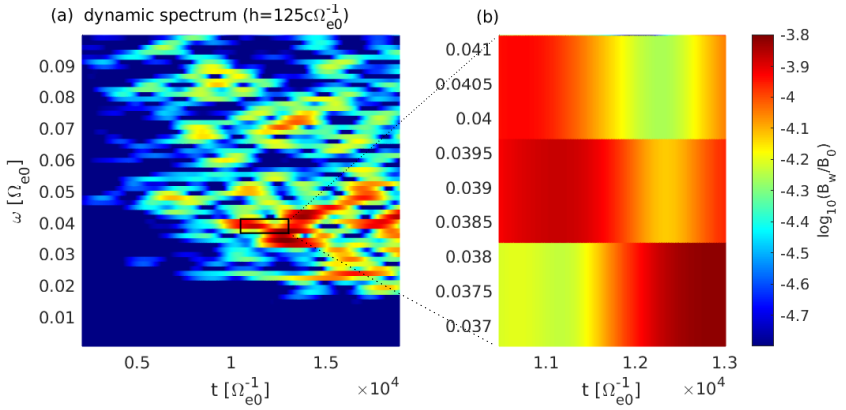

201 **Figure 7.** (a) Dynamic spectrum ($t = 0 \sim 20000\Omega_{e0}^{-1}$) for forward-propagating waves at $h = 125c\Omega_{e0}^{-1}$, the
202 part indicated by the black rectangle is enlarged in panel (b), which corresponds to the first selected mode in
203 Figure 5; (b) a falling-tone structure is well-illustrated.

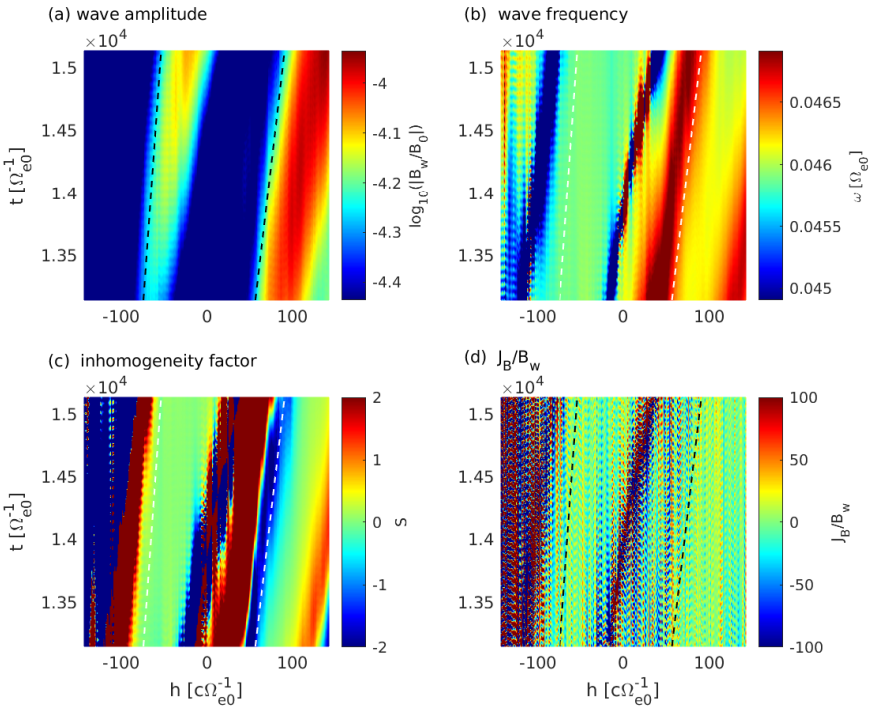

222 **Figure 8.** Spatial and temporal evolution of amplitudes, frequencies, S values, and J_B/B_w for the second
223 selected mode in Figure 5, in which a band-pass filter of $0.045 \sim 0.047\Omega_{e0}$ corresponding to the wavenumber
224 range of the mode is applied. The approximate ends of the left and right wave packets are indicated by dashed
225 lines in each panel.

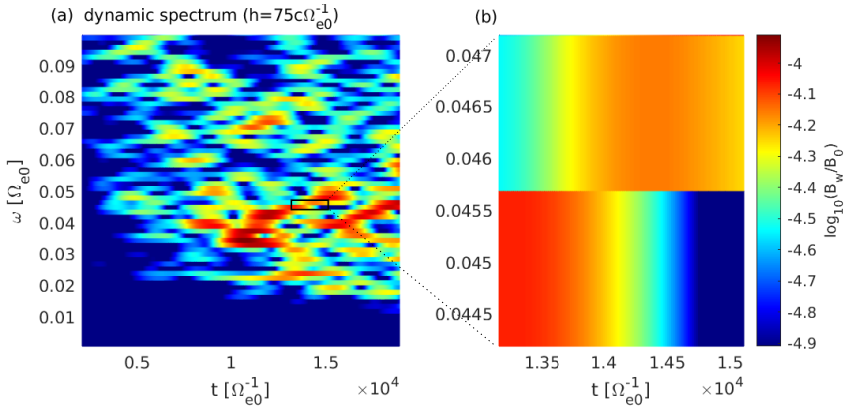

226 **Figure 9.** (a) Dynamic spectrum ($t = 0 \sim 20000\Omega_{e0}^{-1}$) for forward-propagating waves at $h = 75c\Omega_{e0}^{-1}$, the
227 part indicated by the black rectangle is enlarged in panel (b), which corresponds to the second selected mode
228 in Figure 5; (b) a rising-tone structure is well-illustrated.

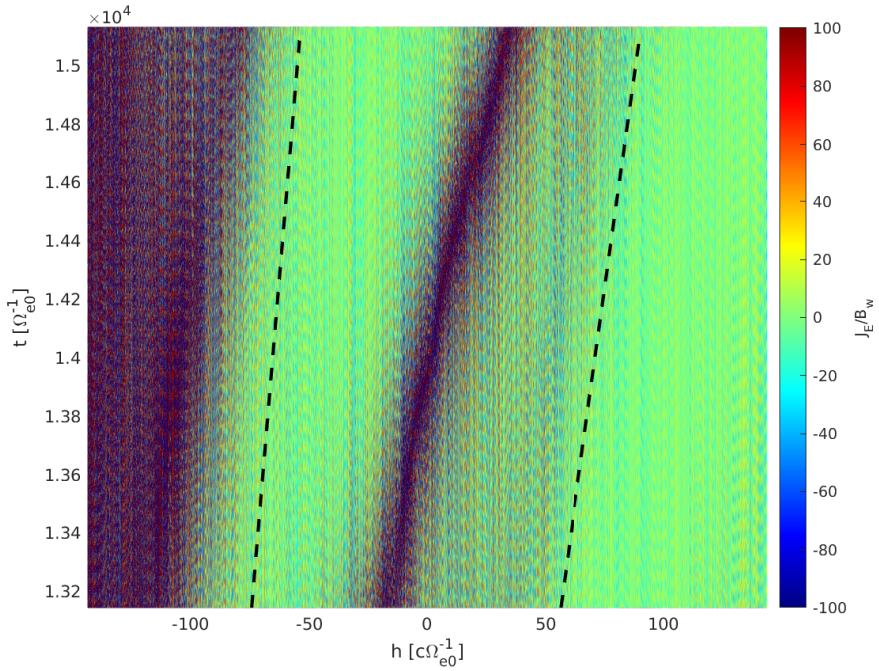

Figure 10. J_E/B_w corresponding to the spatial and temporal ranges of the second selected mode in Figure 5, where a band-pass filter of $0.045 \sim 0.047\Omega_{e0}$ is applied. The black dashed lines indicate the approximate ends of the left and right packets. Much denser positive J_E are found between two wave packets, representing waves in this region are being damped.

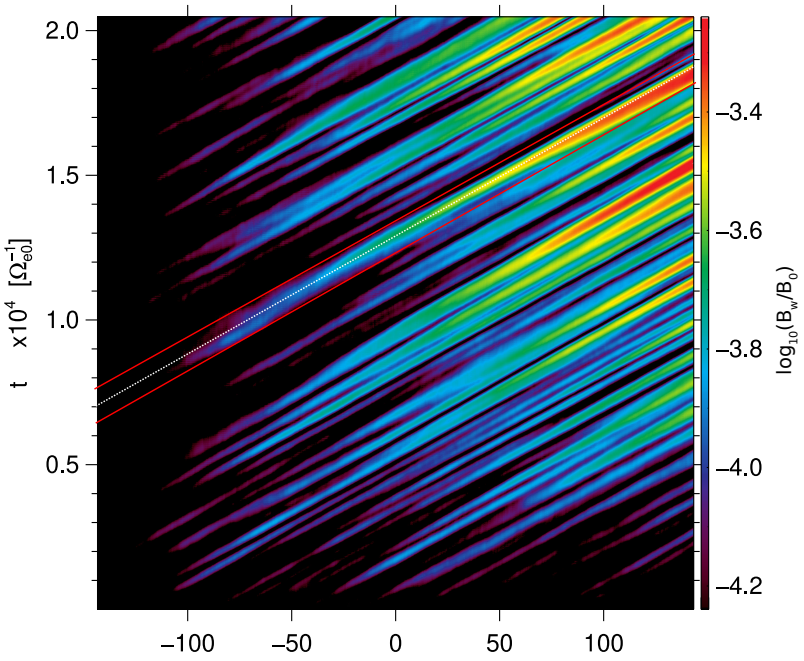

Figure 11. Spatial and temporal evolution of amplitudes ($t = 0 \sim 20000\Omega_{e0}^{-1}$) for forward-propagating waves in a uniform magnetic environment, in which a band-pass filter of $0.04 \sim 0.06\Omega_{e0}$ is applied. The packet bounded by the red lines is extracted for the further analysis. The white dotted line represents the center of the packet.

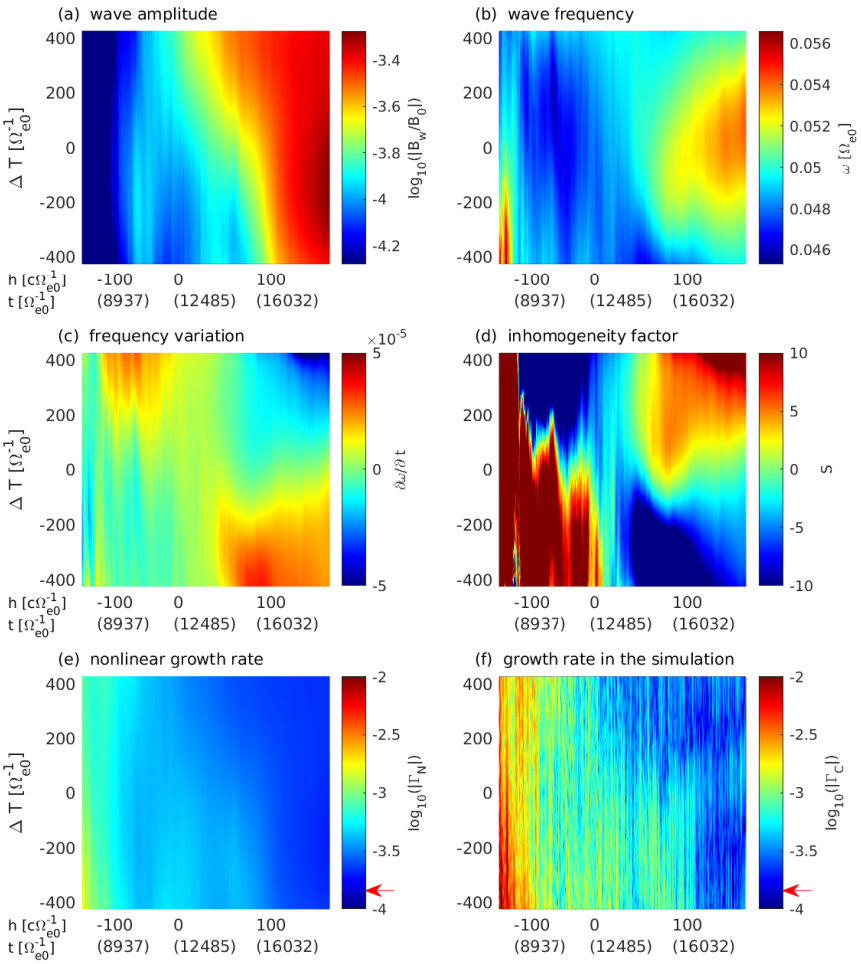

277 **Figure 12.** Amplitudes, frequencies, frequency variations, S values, nonlinear growth rates, and growth
278 rates in the simulation for the extracted wave packet in Figure 11, respectively, as observed in a frame of refer-
279 ence moving with the group velocity. The value of ΔT represents a time deviation from the center ($\Delta T = 0$).
280 The holizontal axis under each panel shows a position in the simulation system, while the time information
281 inside brackets indicates the moment of passing the position. The theoretical linear growth rate under the
282 same condition is represented by red arrows in panels (e) and (f).

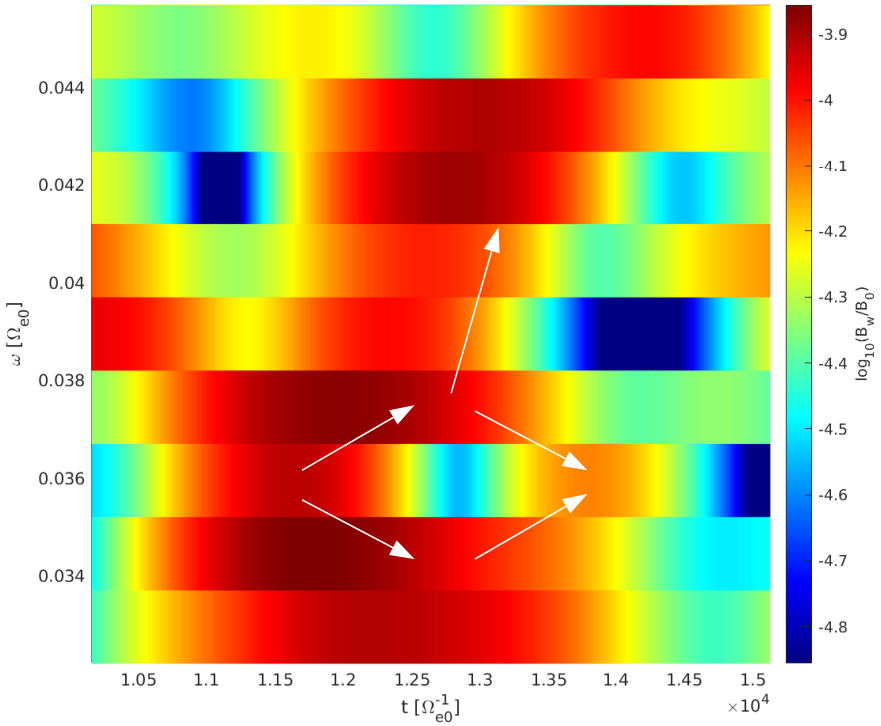

316 **Figure 13.** Dynamic spectrum for forward-propagating waves within $t = 10159 \sim 15123\Omega_{e0}^{-1}$ and $\omega =$
317 $0.032 \sim 0.046\Omega_{e0}$ at $h = 100c\Omega_{e0}^{-1}$ in a uniform background magnetic environment, where obvious merging
318 and splitting of wave packets can be found, as indicated by white arrows.